

Cite this: *Nanoscale*, 2025, 17, 4444

## *In situ* synthesis of a UIO-66-NH<sub>2</sub>@Ti<sub>3</sub>C<sub>2</sub> composite for advanced electrochemical detection of acetaminophen†

 Muhammad Hussnain Afzal,<sup>a</sup> Wajeeha Pervaiz,<sup>b</sup> Zhuo Huang,<sup>c</sup> Zhengyun Wang,<sup>a</sup> Guangfang Li \*<sup>a</sup> and Hongfang Liu \*<sup>a</sup>

Acetaminophen (AP) is a widely used analgesic and antipyretic drug, but its excessive use poses health risks and contributes to environmental contamination. In response to the need for rapid, accurate, and cost-effective detection methods, we developed a highly sensitive and selective electrochemical sensor for AP. The sensor was based on a composite of UIO-66-NH<sub>2</sub> (UN) and an MXene (Ti<sub>3</sub>C<sub>2</sub>). UIO-66-NH<sub>2</sub> was *in situ* synthesized onto the MXene *via* a one-step hydrothermal process with a varying MXene content, followed by calcination at 300 °C under an argon (Ar) flow. This treatment induced the formation of TiO<sub>2</sub> on the MXene surface and increased the interlayer spacing, which enhanced its electrochemical performance. The resulting UN@Ti<sub>3</sub>C<sub>2</sub>-C electrode exhibited remarkable electrochemical activity due to the high surface area and excellent conductivity of the MXene. The fabricated sensor demonstrated a simple yet effective approach for the rapid and quantitative detection of AP, with a linear detection range of 0.032–160 μM and a low detection limit of 10 nM. Moreover, the sensor was successfully applied to detect AP in different water samples, validating its potential as a reliable and efficient tool for AP monitoring.

Received 24th October 2024,  
Accepted 13th January 2025

DOI: 10.1039/d4nr04388j

rsc.li/nanoscale

## 1. Introduction

The global outbreak of the novel coronavirus disease 2019 (COVID-19) caused by severe acute respiratory syndrome coronavirus-2 (SARS-CoV-2) has posed unprecedented challenges to public health systems worldwide. Amidst the urgency to identify effective therapeutic strategies to combat the pandemic, existing drugs with potential repurposing opportunities have garnered significant attention. Among these, AP has emerged as a frontline candidate for managing symptoms associated with COVID-19.

AP also known as paracetamol is a commonly available over-the-counter drug with antipyretic and analgesic pro-

erties.<sup>1</sup> Its affordability, accessibility and relative safety profile have contributed to its widespread usage during the COVID-19 pandemic. AP therapy has a low side-effect frequency, but an overdose can cause liver damage<sup>2,3</sup> and lead to acute hepatic injury.<sup>4,5</sup> In addition, AP has been identified as an aquatic pollutant with traces commonly found in water bodies and fish, stemming from both pharmaceutical manufacturing and human consumption.<sup>6</sup> The concentrations of AP found in the coastal area samples were 75.7–169.8 ngL<sup>-1</sup> which was twice as high as the previously reported concentration before COVID-19 (4.7–72.3 ngL<sup>-1</sup>).<sup>7</sup> Evaluating toxicity in fish stands out as one of the most reliable approaches for comprehending the harmful impacts of environmental pollutants on aquatic ecosystems.<sup>8,9</sup> Therefore, simple, reliable, and sensitive methods need to be developed for AP detection.

There are many commonly used techniques for the detection of AP, including high-performance liquid chromatography (HPLC),<sup>10</sup> gas chromatography (GC),<sup>11</sup> spectrophotometry,<sup>12</sup> thermogravimetric analysis, and electrochemical methods.<sup>13,14</sup> However, these methods have drawbacks, including low selectivity, complex procedures, high costs and the need for sample pre-treatment. In contrast, researchers are increasingly attracted to electrochemical sensing technology due to its extensive applicability in the analysis of environmental and biological data. This fascination stems from its notable advan-

<sup>a</sup>Hubei Key Laboratory of Material Chemistry and Service Failure, Key Laboratory of Material Chemistry for Energy Conversion and Storage (Ministry of Education), Hubei Engineering Research Center for Biomaterials and Medical Protective Materials, School of Chemistry and Chemical Engineering, Huazhong University of Science and Technology, 1037 Luoyu Rd, Wuhan, China.

E-mail: guangFL@hust.edu.cn, liuhfj@hust.edu.cn

<sup>b</sup>College of Food Science and Technology, Huazhong Agricultural University, 1 Shizishan Street, Wuhan, China

<sup>c</sup>Changjiang River Scientific Research Institute of Changjiang Water Resources Commission, 289 Huangpu Street, Wuhan, Hubei, China

† Electronic supplementary information (ESI) available. See DOI: <https://doi.org/10.1039/d4nr04388j>

tages, including sensitivity and excellent selectivity, rapid analytical response, straightforward equipment requirements, cost-effectiveness and the absence of sample pre-treatment requirements.<sup>15–17</sup>

So far, a variety of materials with distinctive electrochemical properties have been explored for the development of electrochemical sensors aimed at detecting AP. These materials include graphene,<sup>18</sup> graphene oxide,<sup>19</sup> carbon nanotubes,<sup>20</sup> metal nanoparticles,<sup>21</sup> and MXenes,<sup>22,23</sup> as well as metal-organic frameworks (MOFs) and MOF-derived carbon materials.<sup>24,25</sup> Among these options, MOFs have gained attention due to their diverse structure, ample specific surface area and uniformly structured cavities. MOFs have proven to be excellent sacrificial templates for creating innovative metal or metal oxide nano-porous carbon composites. However, the low electrical conductivity of MOFs hinders electron transfer, restricting their use in certain applications such as electrochemical sensors. Several works have recently shown the potential of MOFs for electrochemical sensing. For example, Tang *et al.*<sup>26</sup> developed a Co-based MOF which shows good electrocatalytic performance for AP with a glassy carbon electrode. Among all the MOFs, UIO-66-NH<sub>2</sub> (Zr-MOF) is the promising candidate for electrochemical sensing in aqueous media, the property of the material to be considered should be its water stability.<sup>27,28</sup> Its highly porous nature provides sites for the analyte molecules and consequently improves the sensitivity of the electrochemical sensing system. Zhang *et al.*<sup>29</sup> developed an electrochemical sensor using Zr-MOF and carbon derived from walnut shells (WC) as modified materials. This sensor is highly sensitive and selective for detecting paracetamol (Para) and *para*-aminophenol (PAP). Furthermore, Li *et al.*<sup>24</sup> further improved the sensing performance for AP and dopamine by combining Zr-MOF with carbon nanotubes.

MXenes are novel two-dimensional (2D) nanomaterials similar to graphene, consisting of multiple layers. They have excellent electrical conductivity, a large specific surface area and

numerous functional groups making them highly attractive in the field of electrochemistry.<sup>30</sup> MXenes are typically represented by the formula  $M_{n+1}X_nT_x$ , where “M” stands for transition metals, “X” refers to carbon or nitrogen atoms, and “T<sub>x</sub>” indicates surface functional groups like –OH, –O, and –F. MXenes can establish strong interactions with the organic ligands found in MOFs and some inorganic compounds due to their multiple active sites.<sup>31</sup> They are particularly effective as a conductive platform to support materials that have high catalytic activity but low electrical conductivity. As a result,  $Ti_3C_2T_x$ -MXene is widely used in electrochemical sensing applications.<sup>32</sup> For example, Zhao *et al.*<sup>33</sup> developed a disposable electrochemical biosensor using multi-dimensional nanocomposites (MXene/Au–Pd) to detect organophosphorus pesticides. In another study, Wang and colleagues created an electrochemical sensor based on a reduced graphene oxide (rGO) and  $Ti_3C_2T_x$ -MXene composite, specifically for the detection of AP.<sup>34</sup> These examples demonstrate the versatility and effectiveness of  $Ti_3C_2T_x$ -MXene in enhancing the sensor performance in various applications.

In this study, UN@ $Ti_3C_2$ -C was synthesized by a hydrothermal method with a varying content of MXene (20, 30, 50 and 70% by weight) and then calcined to 300 °C under an argon atmosphere resulting in the formation of  $TiO_2$  on the MXene surface as presented in Fig. 1. This process improved its conductivity and increased its surface area. The electrochemical behavior of AP was tested using the UIO-66-NH<sub>2</sub> and MXene composites. The results showed that this electrochemical sensor could detect AP with high sensitivity, selectivity, and stability. Moreover, it was effective in detecting AP in real-world samples.

## 2. Experimental section

### 2.1 Chemicals and materials

MAX phase ( $Ti_3AlC_2$ ), lithium fluoride (LiF), hydrochloric acid (HCl), zirconium chloride ( $ZrCl_4$ ), 2-amino terephthalic acid

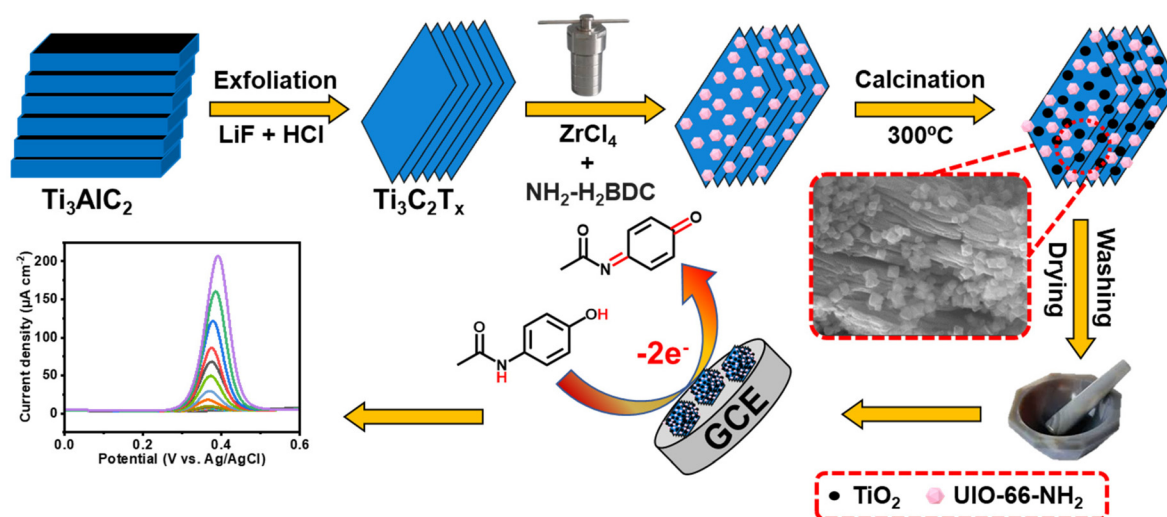


Fig. 1 Schematic diagram of the various steps in UIO-66-NH<sub>2</sub>@Ti<sub>3</sub>C<sub>2</sub>-C synthesis and the electrochemical sensing mechanism.

(2-NH<sub>2</sub>-BDC), acetic acid (CH<sub>3</sub>COOH), dimethylformamide (DMF), and methanol (CH<sub>3</sub>OH) reagents were purchased from Sinopharm Group Chemical Reagent Co. Ltd (Shanghai, China). All of the chemicals were analytically pure and used without any further purification. Double distilled water was used to make all of the solutions. The supporting electrolyte of 0.1 M phosphate buffer solution (PBS, pH = 7) was composed of KH<sub>2</sub>PO<sub>4</sub> and K<sub>2</sub>HPO<sub>4</sub>·3H<sub>2</sub>O in a suitable amount, and it was used throughout the experiment.

## 2.2 Instrumentation

X-ray diffraction patterns (XRD) were obtained using a Rigaku D/max-rA diffractometer (Japan) with a Ni filter using Cu K $\alpha$  radiation (40 kV, 200 mA), and X-ray photoelectron spectroscopy (XPS) was carried out on an AXISULTRA DLD-600 W X spectrometer (Shimadzu Company). Scanning electron microscopy (SEM) was performed on a HITACHI X-650 (Hitachi Co., Japan). An acceleration voltage of 200 kV was used to capture the images of transmission electron microscopy (TEM) with a TECNAI G220 U-Twin instrument (Netherlands). Cyclic voltammetry (CV), differential pulse voltammetry (DPV), and electron impedance spectroscopy (EIS) were performed on a CHI760E electrochemical workstation (CH Instrument Company, Shanghai, China), and fitted with GCE, Ag/AgCl/saturated KCl, and platinum as the working, reference, and counter electrodes respectively, in a traditional three-electrode system at room temperature with deoxygenated 10 mL of 0.1 M PBS (pH = 7). The working potential range was used from -0.6 to 1.2 V in CV and DPV, while a frequency range of 0.1 to 10<sup>5</sup> Hz and 0.005 V of sinusoidal potential amplitude were established for EIS.

## 2.3 Preparation of MXene (Ti<sub>3</sub>C<sub>2</sub>)

MXene was prepared by etching 1 g Ti<sub>3</sub>AlC<sub>2</sub> powder with a mixture of 1 g LiF and HCl (10 mol L<sup>-1</sup>, 20 ml) in a container for 30 h under stirring for removal of the Al layer based on previous literature.<sup>35</sup> Afterwards, deionized water was utilized to wash the mixture, effectively removing any remaining acid and impurities. Subsequently, the obtained solid sample was added to deionized water again using a sonication process for 6 h under N<sub>2</sub> flow. Finally, after freeze-drying for 24 h, the final product was obtained.

## 2.5 Preparation of UN@Ti<sub>3</sub>C<sub>2</sub>

Preparation of UN@Ti<sub>3</sub>C<sub>2</sub> was as follows: 50 mg of ZrCl<sub>4</sub> and 50 mg of 2-NH<sub>2</sub>-BDC were dissolved in 20 ml DMF by vigorously stirring and it was named solution A. Then 20, 30, 50 and 70% by weight of the above-mentioned Ti<sub>3</sub>C<sub>2</sub> were dispersed ultrasonically in 20 mL DMF separately for 30 minutes and named solution B. Solution A was added to solution B to obtain solution C. Then, 10 ml of acetic acid was further added to solution C under persistent mechanical stirring for 30 minutes. Next, these four suspensions were transferred to a Teflon-lined stainless-steel autoclave and heated for 16 h at 120 °C. After that, the powder form was separated and methanol was used to wash it several times and dried at 60 °C overnight. This process yielded various compositions of UN@Ti<sub>3</sub>C<sub>2</sub> with ratios of 20%, 30%,

50%, and 70%. Additionally, UiO-66-NH<sub>2</sub> was synthesized using the same procedure but without the inclusion of MXene.

## 2.5 Preparation of UiO-66-NH<sub>2</sub>@Ti<sub>3</sub>C<sub>2</sub>-C

The UN@Ti<sub>3</sub>C<sub>2</sub>-C composite was obtained by a simple calcination method. Typically, the above-prepared (20, 30, 50 and 70%) UN@Ti<sub>3</sub>C<sub>2</sub> was calcined at 300 °C at a ramping rate of 5 °C min<sup>-1</sup> in an Ar flow to obtain UN@Ti<sub>3</sub>C<sub>2</sub>-C. Finally, the obtained samples were collected and ground.

## 2.6 Modification of the glassy carbon electrode (GCE)

An alumina slurry with particle sizes of 0.3 and 0.05  $\mu$ m was poured onto micro cloth pads and used to polish and modify the surface of the GCE, which has a diameter of 3 mm. In the next step, it was washed with distilled H<sub>2</sub>O and ethanol for one minute ultrasonically and finally, N<sub>2</sub> was purged to dry it. Afterward, 5  $\mu$ L of each suspension (3 mg mL<sup>-1</sup>), UN, 20% UN@Ti<sub>3</sub>C<sub>2</sub>-C, 30% UN@Ti<sub>3</sub>C<sub>2</sub>-C, 50% UN@Ti<sub>3</sub>C<sub>2</sub>-C, and 70% UN@Ti<sub>3</sub>C<sub>2</sub>-C were cast on a polished GCE surface at ambient temperature.

# 3. Results and discussion

## 3.1 Characterization of 50% UN@Ti<sub>3</sub>C<sub>2</sub>-C

Firstly, we performed SEM and TEM to investigate the morphology of UiO-66-NH<sub>2</sub>, UN@Ti<sub>3</sub>C<sub>2</sub>, and 50% UN@Ti<sub>3</sub>C<sub>2</sub>-C samples, as shown in Fig. 2(A-E). Fig. 2(A) shows the successful synthesis of octahedral UiO-66-NH<sub>2</sub> with particle sizes ranging from 0.33  $\mu$ m to 0.52  $\mu$ m and an average size of 0.45  $\mu$ m. Fig. 2(B) demonstrates the successful integration of octahedral UiO-66-NH<sub>2</sub> onto the MXene surface. Fig. 2(C) shows the SEM images of 50% UN@Ti<sub>3</sub>C<sub>2</sub>-C, revealing MXene layers with octahedral UiO-66-NH<sub>2</sub> positioned on and between these layers. A significant amount of TiO<sub>2</sub> was observed on the surface of MXene, which increased the thickness of the layers and the interlayer spacing, and the MXene surface became rougher due to the conversion of Ti<sub>3</sub>C<sub>2</sub> into TiO<sub>2</sub>.<sup>36,37</sup> Fig. 2(D and E) display the TEM image of 50% UN@Ti<sub>3</sub>C<sub>2</sub>-C which shows TiO<sub>2</sub> particles on the MOF surface. Additionally, Fig S1† presents the EDX spectrum of 50% UN@Ti<sub>3</sub>C<sub>2</sub>-C, while Table S1† shows the relative concentrations of different elements present in the material.

Furthermore, XRD analysis was used to examine the crystal-line structure of UiO-66-NH<sub>2</sub>, Ti<sub>3</sub>C<sub>2</sub> and composite materials UN@Ti<sub>3</sub>C<sub>2</sub> and 50% UN@Ti<sub>3</sub>C<sub>2</sub>-C as displayed in Fig. 3(F). The major diffraction peaks at 7.36°, 8.55°, and 25.68° are assigned to the (111), (200), and (422) crystal planes which indicate the successful synthesis of UiO-66-NH<sub>2</sub>.<sup>38</sup> In Ti<sub>3</sub>C<sub>2</sub>, the diffraction peaks at 8.79°, 18.23°, and 27.62° are assigned to the (002), (004), and (006) planes respectively.<sup>35,39</sup> After calcination of 50% UN@Ti<sub>3</sub>C<sub>2</sub> at 300 °C, the diffraction peak at 7.6° slightly shifted to 7.25° indicating an increase in interlayer spacing. In addition to the presence of main characteristic peaks from Ti<sub>3</sub>C<sub>2</sub>, many other peaks are observed for anatase TiO<sub>2</sub> like 25.3°, 37.8°, 48.1°, 53.9°, 55.0°, and 62.7° which were ascribed to the (101), (004), (200), (105), (211), and (204) planes.<sup>40</sup> The

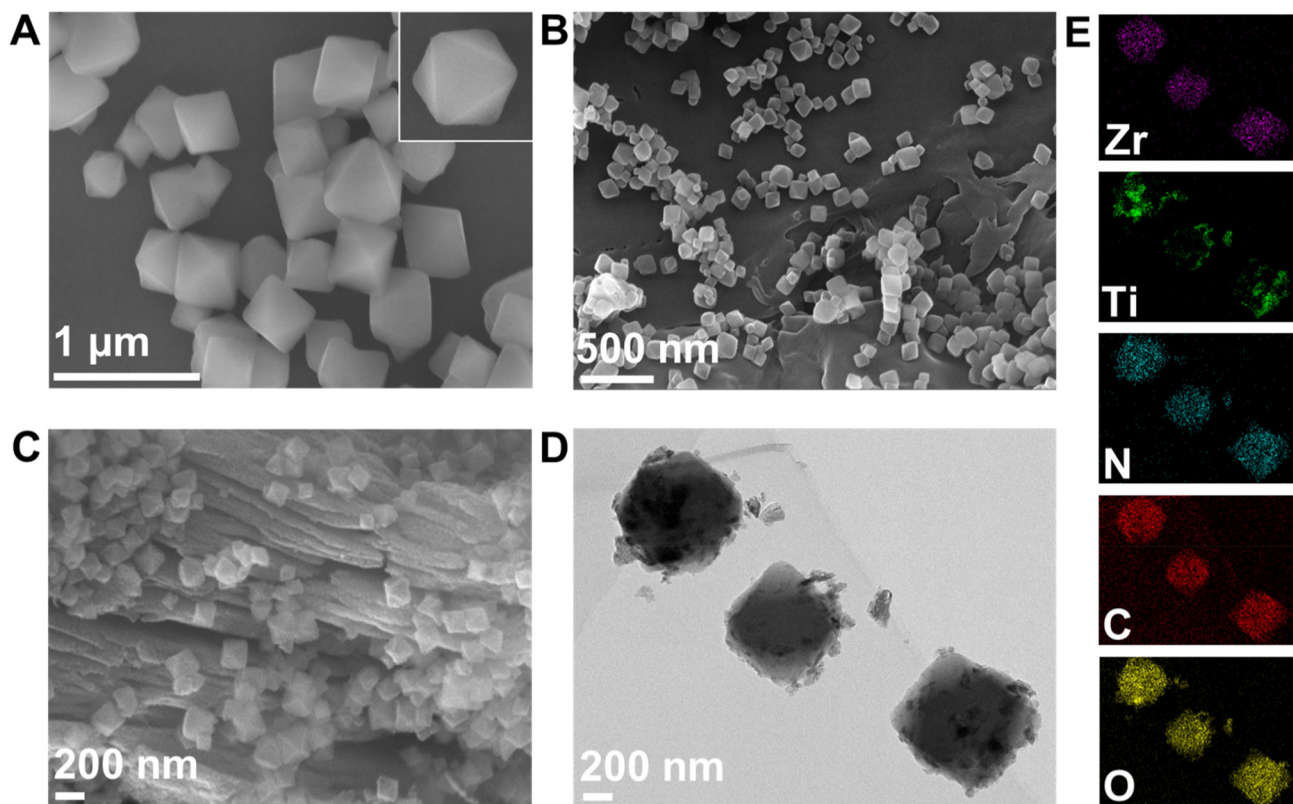


Fig. 2 SEM image of UIO-66-NH<sub>2</sub> (A), UN@Ti<sub>3</sub>C<sub>2</sub> (B), 50% UN@Ti<sub>3</sub>C<sub>2</sub>-C (C), TEM image of 50% UN@Ti<sub>3</sub>C<sub>2</sub>-C (D), the corresponding elemental mapping of 50% UN@Ti<sub>3</sub>C<sub>2</sub>-C (E).

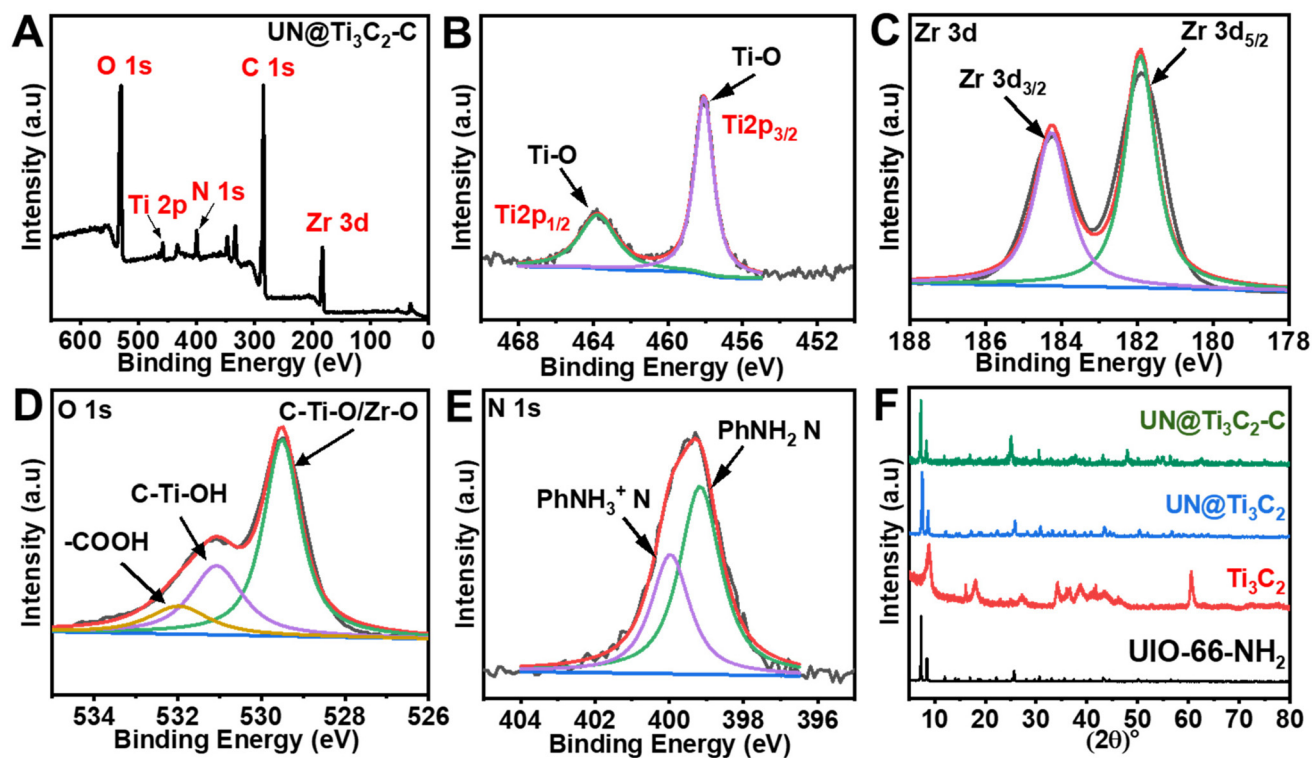


Fig. 3 (A) XPS wide-scan survey spectrum of 50% UN@Ti<sub>3</sub>C<sub>2</sub>-C. (B) Ti 2p. (C) Zr 3d. (D) O 1s. (E) N 1s. (F) XRD patterns of the samples UIO-66-NH<sub>2</sub>, Ti<sub>3</sub>C<sub>2</sub>, UN@Ti<sub>3</sub>C<sub>2</sub>, and UN@Ti<sub>3</sub>C<sub>2</sub>-C.

XRD patterns of UN@Ti<sub>3</sub>C<sub>2</sub> and 50% UN@Ti<sub>3</sub>C<sub>2</sub>-C indicate the successful incorporation of UiO-66-NH<sub>2</sub> on the Ti<sub>3</sub>C<sub>2</sub> surface.<sup>41</sup>

Next, the metallic composition and valence bond configuration of Ti<sub>3</sub>C<sub>2</sub> and UiO-66-NH<sub>2</sub> were studied using XPS. The wide-scan XPS spectrum in Fig. 3(A) indicates the existence of elements like Zr, Ti, N, C and O. Fig. 3(B) depicts the Ti 2p spectrum of 50% UN@Ti<sub>3</sub>C<sub>2</sub>-C which could be fitted into two peaks (Ti 2p<sub>3/2</sub> and Ti 2p<sub>1/2</sub>) that can be ascribed to Ti–O (457.9 and 463.7). The doublet of Ti–O shows the presence of TiO<sub>2</sub> particles. As for the Zr 3d spectrum in Fig. 3(C), two peaks could be attributed to Zr 3d<sub>5/2</sub> and Zr 3d<sub>3/2</sub> with binding energies of 181.9 and 184.2 eV respectively. As for the O 1s spectrum shown in Fig. 3(D), the peak at approximately 529.5 eV is attributed to lattice oxygen (O<sup>2-</sup>) in metal oxides, which likely arises from the partial oxidation of the Ti<sub>3</sub>C<sub>2</sub> surface to form TiO<sub>2</sub> during calcination. Additionally, Zr–O bonds from the UiO-66-NH<sub>2</sub> framework contribute to this peak, indicating the presence of zirconium oxide. The second peak, located

around 531.1 eV, is assigned to surface hydroxyl groups (–OH), which are commonly found on the surface of Ti<sub>3</sub>C<sub>2</sub> as termination groups and may also be present due to interactions between the UiO-66-NH<sub>2</sub> framework and atmospheric moisture. The peak at 532 eV is likely due to carbonyl groups (C=O) from the organic linker in the UiO-66-NH<sub>2</sub> structure, which contains functional groups such as amides or carboxyls.<sup>41,42</sup> As for the N 1s spectrum shown in Fig. 3(E), two peaks are observed at 399.2 eV and 400.1 eV, which can be attributed to the –NH<sub>2</sub> group bonded to the phenyl ring (PhNH<sub>2</sub>) and the protonated amidogen form (PhNH<sub>3</sub><sup>+</sup>), respectively.<sup>43,44</sup> These peaks confirm the presence of the –NH<sub>2</sub> group in the material.

### 3.2 Electrochemical performance of 50% UiO-66-NH<sub>2</sub>@Ti<sub>3</sub>C<sub>2</sub>-C

Electrochemical impedance spectroscopy (EIS) was conducted to assess the interfacial properties of different modified electrodes immersed in a [Fe(CN)<sub>6</sub>]<sup>3-/4-</sup> redox probe solution containing 0.1 M KCl. The electrodes investigated included unmo-

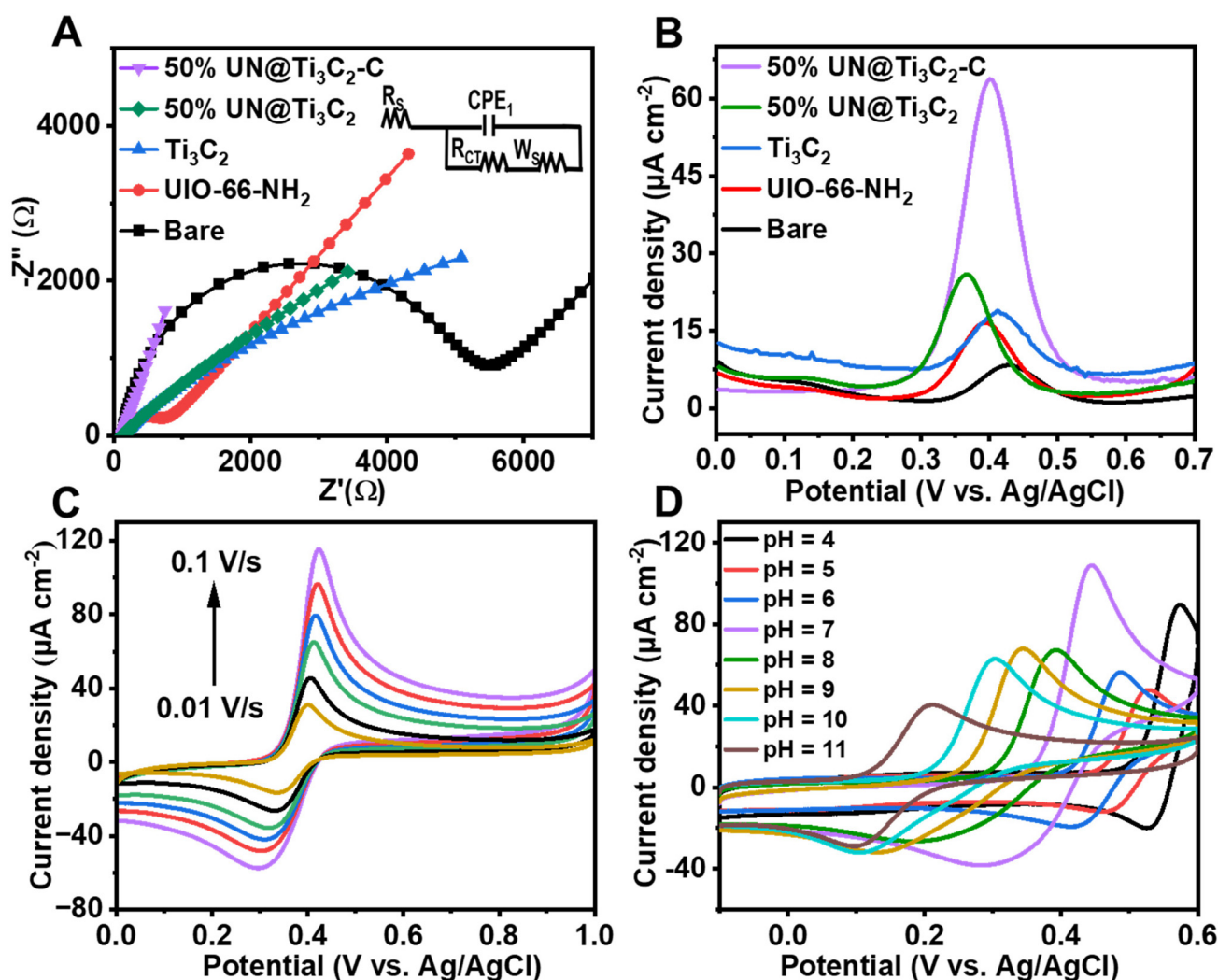


Fig. 4 (A) Nyquist plots of the unmodified and modified electrodes in the 2 mM redox probe of [Fe(CN)<sub>6</sub>]<sup>3-/4-</sup> with 0.1 M KCl, 0.01–10<sup>5</sup> Hz (frequency range). (B) DPV results of various prepared electrodes in 0.1 M PBS with 48 μM AP. (C) Cyclic voltammograms of 50% UN@Ti<sub>3</sub>C<sub>2</sub>-C/GCE at 0.01–0.10 V s<sup>-1</sup> scan rates. (D) Cyclic voltammograms of 50% UN@Ti<sub>3</sub>C<sub>2</sub>-C/GCE in the 48 μM AP solution with various pH.

dified bare GCE, UiO-66-NH<sub>2</sub>/GCE, Ti<sub>3</sub>C<sub>2</sub>/GCE, 50% UN@Ti<sub>3</sub>C<sub>2</sub>/GCE and 50% UN@Ti<sub>3</sub>C<sub>2</sub>-C/GCE. This method was chosen due to its effectiveness in characterizing electrode interfaces. Fig. 4(A) shows different characteristics of Nyquist-plots fitted for the Randle's equivalent circuit (inset of Fig. 4 (A)) where 'R<sub>ct</sub>' stands for the charge transfer resistance of the semicircle, and it controls the kinetics of electrons on the electrode surface while 'R<sub>s</sub>' stands for the resistance of solution, 'C<sub>dl</sub>' stands for double layer capacitance and 'W' denotes the Warburg constant. It can be noticed that the bare GCE shows a large charge transfer resistance with an R<sub>ct</sub> value of 4972.4 Ω. The R<sub>ct</sub> value for UiO-66-NH<sub>2</sub>/GCE is found to be 591.5.7 Ω, reflecting the improved electron transfer due to the MOF's high surface area and porous structure, which facilitate a better interaction between the electrode and electrolyte. For Ti<sub>3</sub>C<sub>2</sub>, the R<sub>ct</sub> value was found to be 130 Ω. When Ti<sub>3</sub>C<sub>2</sub> was incorporated into the composite, the charge transfer resistance decreased with the 50% UN@Ti<sub>3</sub>C<sub>2</sub> composite showing an R<sub>ct</sub> of 105 Ω and the 50% UN@Ti<sub>3</sub>C<sub>2</sub>-C composite further decreasing it to 87 Ω, indicating the optimal balance between the MOF and MXene leading to excellent electron transfer capability. These results highlight the synergistic effect between UiO-66-NH<sub>2</sub> and Ti<sub>3</sub>C<sub>2</sub> in enhancing the electrochemical performance of the electrode. The excellent conductivity and large specific surface area of Ti<sub>3</sub>C<sub>2</sub> combined with the porous nature of UiO-66-NH<sub>2</sub> provide abundant active sites for electron transfer and analyte adsorption. This significantly improves the electrode's sensitivity and efficiency in electrochemical sensing applications. The optimal performance observed with the 50% UN@Ti<sub>3</sub>C<sub>2</sub> composite suggests that balancing the proportion of MXene is crucial for maximizing sensor performance. CV curves of numerous modified electrodes in the redox solution comprising [Fe(CN)<sub>6</sub>]<sup>3-/4-</sup> were recorded and the same results were obtained as shown in Fig S2.† To calculate the effective electroactive surface area of the modified electrode we use the Randles-Sevcik equation.<sup>15,45</sup>

$$I_p = (2.69 \times 10^5) n^{3/2} A C \times D^{1/2} \nu^{1/2}$$

where  $I_p$  represents the peak current,  $n$  is the number of electrons involved in the reaction ( $n = 2$ ),  $A$  is the electroactive surface area (cm<sup>2</sup>),  $D$  is the diffusion coefficient of Fe(CN)<sub>6</sub><sup>3-/4-</sup> and its value is  $7.6 \times 10^{-6}$  cm<sup>2</sup> s<sup>-1</sup>,  $C$  is the concentration of Fe(CN)<sub>6</sub><sup>3-/4-</sup> which is 1 mM and  $\nu$  is scan rate in V s<sup>-1</sup>. The estimated electroactive surface area of 50% UN@Ti<sub>3</sub>C<sub>2</sub>-C/GCE (0.5561 cm<sup>2</sup>) is higher than those of 50% UN@Ti<sub>3</sub>C<sub>2</sub>/GCE (0.2487 cm<sup>2</sup>), Ti<sub>3</sub>C<sub>2</sub>/GCE (0.1247 cm<sup>2</sup>), UiO-66-NH<sub>2</sub>/GCE (0.0971 cm<sup>2</sup>) and bare GCE (0.0684 cm<sup>2</sup>).

To further assess the performance of the electrochemical sensor using six different types of modified electrodes, DPV responses of various modified electrodes, including bare GCE, UiO-66-NH<sub>2</sub>, 50% UN@Ti<sub>3</sub>C<sub>2</sub> and 50% UN@Ti<sub>3</sub>C<sub>2</sub>-C, in 48 μM acetaminophen solution at pH 7 (PBS) are shown in Fig. 4(B). The current density (μA cm<sup>-2</sup>) is plotted against the applied potential (V), demonstrating a clear enhancement in the current response with the addition of MXene. The bare elec-

trode shows the lowest current response, indicating poor sensitivity for acetaminophen detection. The UiO-66-NH<sub>2</sub> modified electrode slightly improves the current signal but the highest sensitivity is observed with the 50% UN@Ti<sub>3</sub>C<sub>2</sub>-C modified electrodes suggesting that this specific composition optimizes the balance between conductivity and active surface area. The incorporation of Ti<sub>3</sub>C<sub>2</sub> improves electron transfer kinetics, while UiO-66-NH<sub>2</sub> provides additional active sites for acetaminophen interaction, resulting in higher sensitivity. Increasing the MXene content from 20% to 50% improves the sensor performance, but beyond 50%, the increase in MXene does not result in further enhancement, as seen in Fig S3.† This suggests that 50% MXene provides the optimal composition for AP sensing.

### 3.3 Influence of pH

The pH of the supporting electrolyte significantly influences the electrochemical characteristics of the working electrode in sensing the target analyte. Hence, we investigated the impact of pH on the response of AP (48 μM) using CV with the 50% UN@Ti<sub>3</sub>C<sub>2</sub>-C/GCE sensor. pH was controlled using 0.1 M PBS, ranging from 4.0 to 11 in CV voltammograms as shown in Fig. 4(D). Notably, the oxidation peak current response for AP was found to be maximal at pH 7.0. Consequently, pH 7.0 was selected as the optimal value for further AP sensing research in this study. Additionally, as illustrated in Fig S4(B),† the oxidation peak potential ( $E_p$ ) of AP exhibited a linear relationship with pH. Specifically, as the pH increased, the linear equations describing this relationship are as follows:

$$E_p = -0.049 \pm 0.002 \text{ pH} + 0.7821 \pm 0.01 \quad (R^2 = 0.9936)$$

The slope values of  $-0.049 \text{ V pH}^{-1}$  were also observed, which is smaller than the Nernst equation calculated value of  $0.059 \text{ V pH}^{-1}$  suggesting that the electrooxidation of AP is a two proton and two electron system.<sup>3,46</sup>

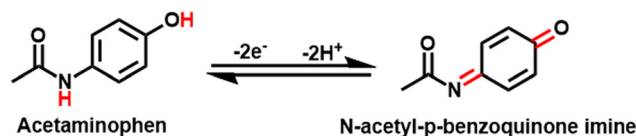
Nernst equation:

$$E_p = E^\theta - \frac{2.303mRT}{nF} \text{pH}$$

where  $E^\theta$  is the conditional potential,  $T$  is the temperature,  $R$  denotes the general gas constant and  $F$  represents Faraday's constant. The  $m/n$  could be determined to be 1.

However, according to the results, the possible mechanism of AP electrochemical sensing is demonstrated in Scheme 1.

Furthermore, for the peak current change,  $I_{pc}$  firstly decreases from 4 to 5 and then increases and at pH 7 it shows



**Scheme 1** Possible mechanism of the electrocatalytic oxidation of acetaminophen at 50% UN@Ti<sub>3</sub>C<sub>2</sub>/GCE.

the maximum current, and thereafter by increasing the pH to 11 the current decreases, as shown in Fig S4(A).†

### 3.4 Influence of scan rate

The effect of scan rate on the current values of AC is investigated at different scan rates from 0.01 to 0.1 V s<sup>-1</sup> with 50% UN@Ti<sub>3</sub>C<sub>2</sub>-C/GCE. As shown in Fig. 4(C), both anodic and cathodic currents increase with the increase in scan rate from 0.01 to 0.1 V s<sup>-1</sup>. To understand how electrode reactions work, a calibration plot is drawn between scan rates and peak current values, as shown in Fig S5(A).† These results confirm that a mass diffusion-controlled process is involved in the AP redox reactions at the surface of 50% UN@Ti<sub>3</sub>C<sub>2</sub>-C/GCE. Moreover, the oxidation peak potential is linearly related to the log of the scan rate and follows the equations  $E_{pa} = 0.042 \pm 0.001 + 0.446 \pm 0.002$  ( $R^2 = 0.9875$ ) and  $E_{pc} = 0.065 \pm 0.005 + 0.257 \pm 0.007$  ( $R^2 = 0.9714$ ), as shown in Fig S5(B).† Based on<sup>47</sup> theory, the value of charge transfer coefficient ( $\alpha$ ) could be found using the following equation.<sup>48</sup>

$$\log \frac{K_a}{K_c} = \log \frac{K_a}{K_c} \text{ or } \frac{K_a}{K_c} = \frac{K_a}{K_c}$$

where  $K_a$  is the slope of  $E_{pa}$  vs.  $\log \nu$  (0.04271) and  $K_c$  is the slope of  $E_{pc}$  vs.  $\log \nu$  (0.0651). According to the formula,  $\alpha$  was calculated to be 0.37. According to<sup>47</sup> theory, the slopes of the lines were equal to  $2.3RT/(1 - \alpha)nF$  and  $-2.3RT/\alpha nF$  for the anodic and cathodic peaks, respectively. The number of electrons involved in the reaction of AP is 2. Furthermore, the heterogeneous electron transfer rate constant ( $k_s$ ) was evaluated according to the following equation:

$$\log K_s = \alpha \log \frac{\alpha}{1 - \alpha} + (1 - \alpha) \log \alpha - \log \frac{RT}{nFv} - \frac{\alpha(1 - \alpha)nF\Delta E_p}{2.3RT}$$

where 'R' stands for the ideal gas constant, F is Faraday's constant,  $\Delta E_p$  is the value for peak potential shift, and n indicates the number of electron transfers. The value of  $k_s$  was calculated to be 1.6745 s<sup>-1</sup> and 1.5936 s<sup>-1</sup> for  $\Delta E_{pa}$  and  $\Delta E_{pc}$  respectively. The high value of  $k_s$  indicates that 50% UN@Ti<sub>3</sub>C<sub>2</sub>-C/GCE could effectively improve the electron transfer between the surface of the electrode and electrolyte solution.<sup>20,45</sup>

### 3.5 Determination of AP (sensitivity)

To investigate the sensitivity of 50% UN@Ti<sub>3</sub>C<sub>2</sub>-C/GCE under optimal conditions following the addition of AP (PBS, pH = 7.0), DPV has been employed. By increasing the concentration of AP, the oxidation peak current values increased constantly as shown in Fig. 5(A). Moreover, Fig. 5(B) shows the calibration plot between AP concentrations and oxidation peak current which matches the linear regression equation  $y = 1.235 \pm 0.01 + 6.455 \pm 0.66$  from 0.032  $\mu$ M to 160  $\mu$ M linear range with  $R^2 = 0.9983$ . The limit of detection (LOD) and limit of quantification (LOQ) were calculated to be 0.010  $\mu$ M and 0.15  $\mu$ M using equations of IUPAC,  $LOD = 3S/m$  and  $LOQ = 10S/m$

respectively. In these equations, S is the standard deviation of blank (no analyte) and m is the slope of the calibration curve. The sensitivity was estimated to be 1.235  $\mu$ A  $\mu$ M<sup>-1</sup> cm<sup>-2</sup> which can be calculated by dividing the slope of the calibration plot by the surface area of the electrode. Furthermore, the analytical performance of the proposed electrochemical sensor based on the 50% UN@Ti<sub>3</sub>C<sub>2</sub>-C composite for AP sensing was compared with traditional methods and previously reported electrochemical sensors in terms of detection method, LOD, and linear range (Table 1). This comparison highlights the superior sensitivity and broader linear range of the proposed sensor, demonstrating its effectiveness in AP detection. By integrating the unique properties of UIO-66-NH<sub>2</sub> and MXene, the sensor exhibits enhanced electrochemical performance providing improved detection limits and selectivity compared to traditional sensors.

### 3.6 Selectivity, reproducibility, and stability

To determine the selectivity of 50% UN@Ti<sub>3</sub>C<sub>2</sub>-C/GCE, we perform DPV measurements against different possible interfering species including dopamine, ascorbic acid, nicotinic acid, L-histidine, lauric acid, glucose, citric acid, anions and cations that may cause interference. A distinctive response can be seen in Fig. 5(C) upon the addition of 48  $\mu$ M AP in 0.1 M PBS at pH 7.0. In the potential window of -0.1 to 0.6, a 10-fold higher concentration of each of the species does not show any significant interference. Dopamine and ascorbic acid show peaks but they do not show a significant effect on AP's current peak. So, the mentioned results confirmed that this sensor is highly selective. The reproducibility tests were carried out in 0.1 PBS containing 40  $\mu$ M AP under the same experimental conditions.  $I_{pa}$  was measured at the five different electrodes through DPV and relative standard deviation (RSD) was calculated to be 1.34% as illustrated in Fig. 5(D). Furthermore, the sensor's stability was examined by storing the electrode for periods of 7, 15, and 21 days before use, and the peak currents achieved were 98.1% (RSD = 0.72%), 97.6% (RSD = 1.09) and 96.8% (RSD = 1.62%) of the initial current signal, respectively, as shown in Fig S6.† The results demonstrate the good reproducibility and stability of this sensor.

### 3.7 Mechanism

The synthesis of a UN/Ti<sub>3</sub>C<sub>2</sub> composite, followed by calcination at 300 °C under an argon atmosphere, offers an efficient approach for the electrochemical detection of AP. UIO-66-NH<sub>2</sub>, a MOF formed by Zr<sup>4+</sup> ions and 2-aminoterephthalic acid, provides high porosity and amine groups that enhance AP adsorption. Ti<sub>3</sub>C<sub>2</sub> contributes superior conductivity and functional groups (-OH, =O) that improve electron transfer during sensing.

During synthesis, MXene integrates with or attaches to the MOF, enhancing dispersion and performance. Calcination stabilizes the composite, retaining the MOF's porosity and amine functionality while dehydrating MXene and partially modifying its surface groups. Minor TiO<sub>2</sub> formation during

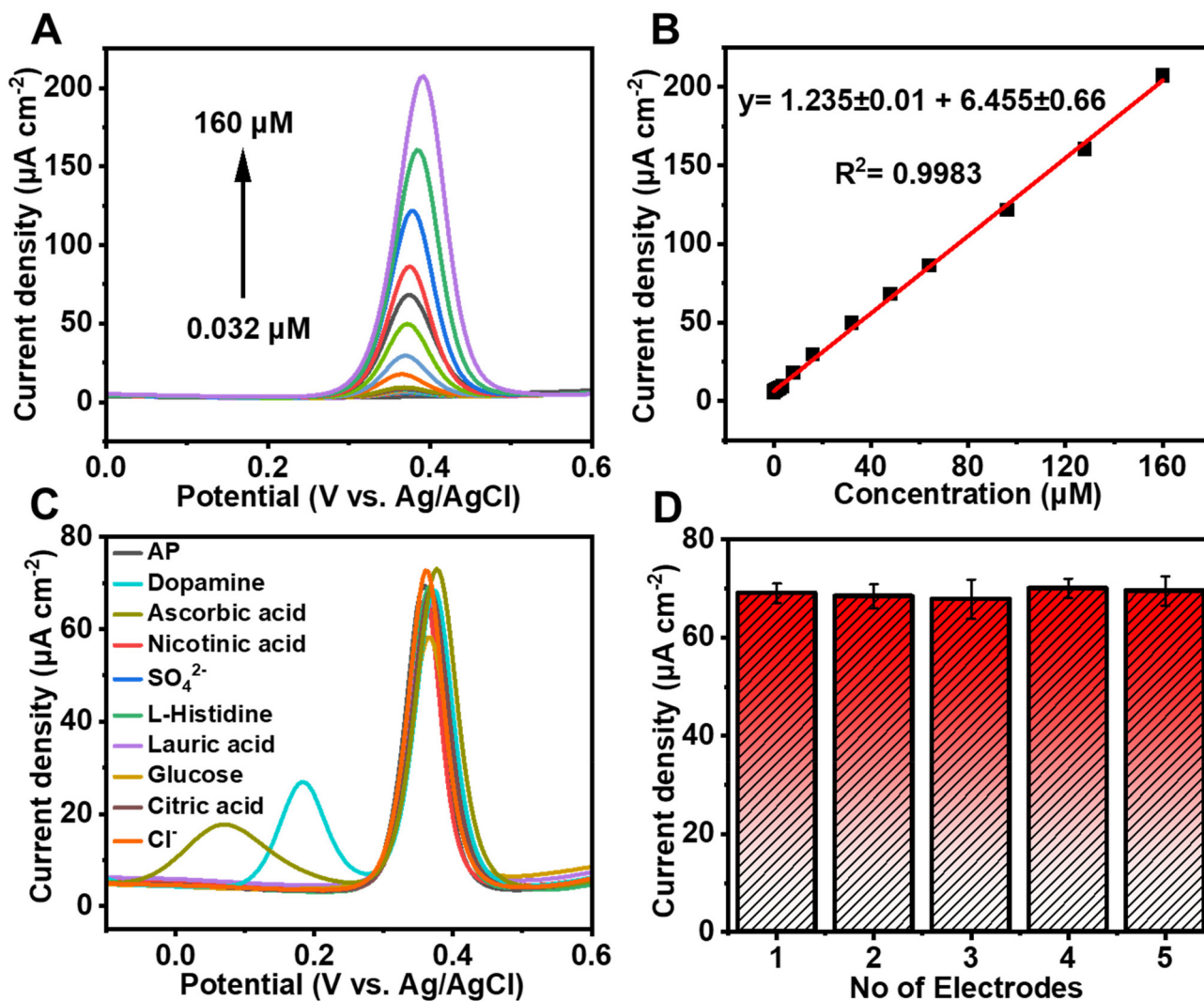


Fig. 5 (A) DPV curves of UN@TT-C/GCE with different AP concentrations from 0.032 to 160  $\mu\text{M}$  in 0.1 M PBS with pH 7.0. (B) Current density ( $\mu\text{A cm}^{-2}$ ) vs. concentration ( $\mu\text{M}$ ) linear calibration plot of AP. (C) DPV of 48  $\mu\text{M}$  AP in 0.1 M PBS (pH = 7.0) using 50% UN@Ti<sub>3</sub>C<sub>2</sub>-C/GCE with 10-time dosage of the different interference species. (D) Reproducibility graph of five electrodes.

calcination strengthens the composite *via* Zr–O–Ti bonds, with additional hydrogen bonding enhancing structural stability.

The composite's high surface area and functional groups enable effective AP adsorption through hydrogen bonding and  $\pi$ – $\pi$  interactions, and the amine groups ( $-\text{NH}_2$ ) in UIO-66-NH<sub>2</sub> act as adsorption sites for acetaminophen. The  $-\text{NH}_2$  groups form hydrogen bonds with the hydroxyl ( $-\text{OH}$ ) group on the AP molecule. The aromatic ring of the 2-aminoterephthalic acid linker interacts with the aromatic ring of AP through  $\pi$ – $\pi$  stacking, further stabilizing the adsorption. Zr<sup>4+</sup> ions act as catalytic sites in this system due to their Lewis acidic properties, which enables coordination with the electron-rich hydroxyl and amino groups of acetaminophen. This coordination enhances the electrophilicity of the AP molecule, facilitating the oxidation process to the reactive metabolite *N*-acetyl-*p*-benzoquinone imine (NAPQI). The Zr<sup>4+</sup> ions can also stabilize the transition states during oxidation, lowering the activation

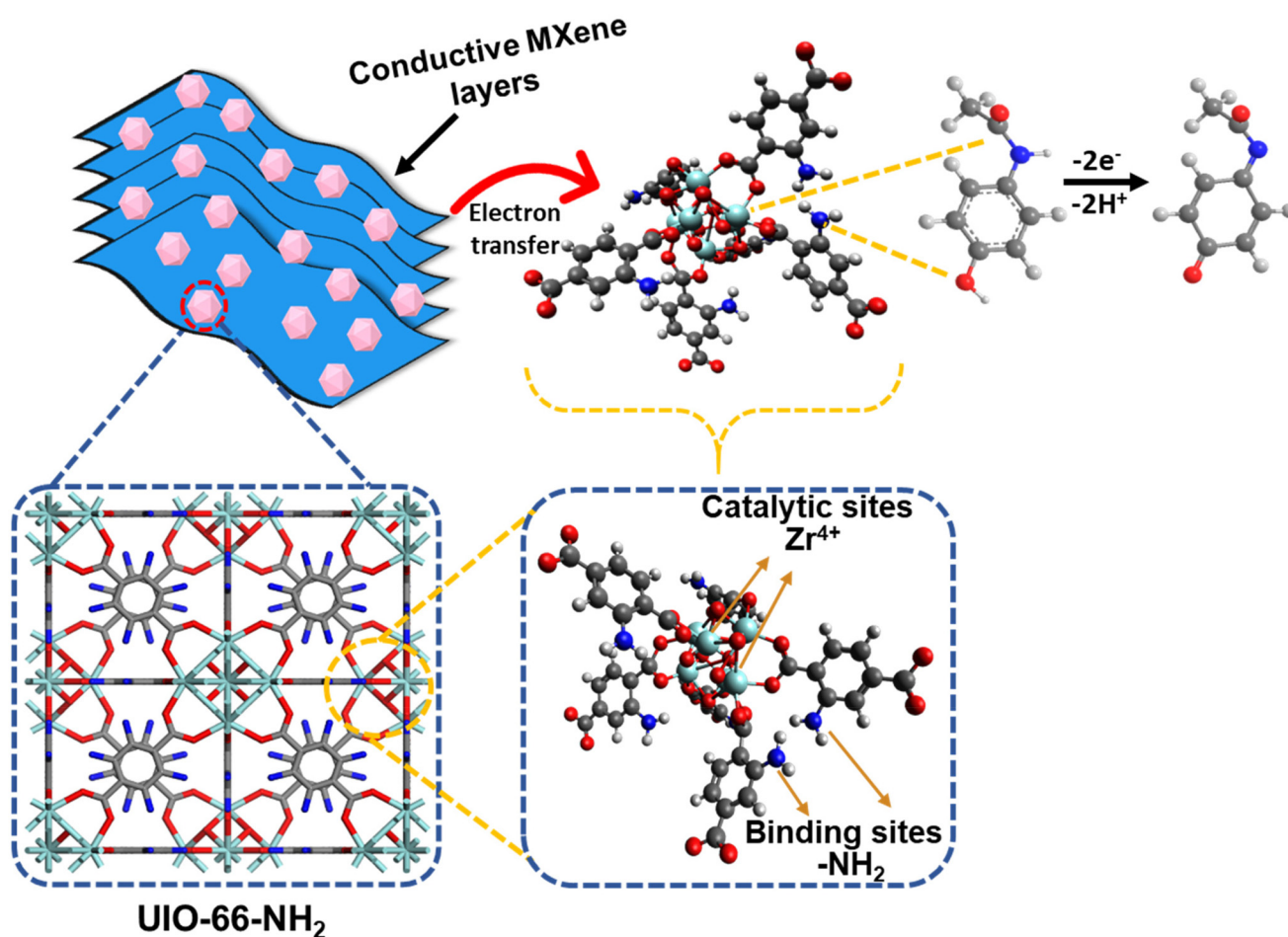
energy and promoting faster electron transfer.<sup>59,60</sup> Moreover, Ti<sub>3</sub>C<sub>2</sub> ensures fast electron transfer during the oxidation of AP to NAPQI as presented in Fig. 6. The presence of TiO<sub>2</sub>, formed during calcination, further enhances the catalytic activity by providing additional sites for electron transfer, contributing to the overall efficiency of the sensor. This combination creates a robust, reusable sensor material with high sensitivity and selectivity, suitable for practical applications and further optimization.

### 3.8 Determination of acetaminophen in real samples

To assess the practical utility of the fabricated 50% UN@Ti<sub>3</sub>C<sub>2</sub>-C sensor, recovery experiments were conducted using real-world water samples collected from tap water, the Yangtze River, and East Lake. The standard addition method was employed for the recovery experiments, where two concentrations of AP (10  $\mu\text{M}$  and 20  $\mu\text{M}$ ) were added to three different

**Table 1** Comparison of different modified electrodes with 50% UN@Ti<sub>3</sub>C<sub>2</sub>-C/GCE for sensitive AP determination

Traditional methods				
Method	LOQ	LOD	Linear range	Ref.
UV spectrophotometry	0.0869 $\mu\text{g mL}^{-1}$	0.0287 $\mu\text{g mL}^{-1}$	2–10 $\mu\text{g mL}^{-1}$	49
GC-MS	20.00 $\mu\text{g mL}^{-1}$	6.00 $\mu\text{g mL}^{-1}$	75–500 $\mu\text{g mL}^{-1}$	50
HPLC	$1.7 \times 10^6$ M	$5 \times 10^7$ M	10 $\mu\text{g L}^{-1}$ –5 $\text{mg L}^{-1}$	51
HPLC	0.11 $\mu\text{g mL}^{-1}$	0.04 $\mu\text{g mL}^{-1}$	1–300 $\mu\text{g/mL}$	52
HPLC	0.2 $\mu\text{g mL}^{-1}$	0.067 $\mu\text{g mL}^{-1}$	0.2 $\mu\text{g mL}^{-1}$ –75 $\mu\text{g mL}^{-1}$	53
HPLC	2.13 $\mu\text{g mL}^{-1}$	0.64 $\mu\text{g mL}^{-1}$	10–400 $\mu\text{g mL}^{-1}$	50
Electrochemical sensors				
Sensor material	Detection method	LOD ( $\mu\text{M}$ )	Linear range ( $\mu\text{M}$ )	Ref.
Co–N–C@PC/GCE	DPV	0.034	0.1–25	54
N–HKUST–1/Au/GCE	DPV	0.16	1–4448.4	55
ZnO–MoO <sub>3</sub> -C/SPE	DPV	1.14	2.5–2000	56
MXene/SPE	DPV	0.048	0.25–2000	57
Ti <sub>3</sub> C <sub>2</sub> T <sub>x</sub> /MWCNT/GCE	DPV	0.23	1.0–90.1	58
UiO-66-NH <sub>2</sub> /CNTs/GCE	DPV	0.009	0.03–2.0	24
50% UN@Ti <sub>3</sub> C <sub>2</sub> -C/GCE	DPV	0.010	0.032–160	This work

**Fig. 6** Schematic representation of the sensing mechanism for AP using the UN@Ti<sub>3</sub>C<sub>2</sub>-C composite electrode.

**Table 2** DPV and HPLC measured results of AP in tap water, river water and lake water samples

Samples	Added ( $\mu\text{M}$ )	Found ( $\mu\text{M}$ )	Recovery (%)	RSD (% , $n = 3$ )
Tap water	10	9.85	98.5	$\pm 1.69$
	20	19.82	99.1	$\pm 1.87$
Yangtze river	10	10.3	103	$\pm 2.63$
	20	20.7	102.7	$\pm 1.98$
East lake	10	11.15	111.5	$\pm 3.52$
	20	21.45	107.2	$\pm 2.83$

water samples. As shown in Table 2, the recovery rates for AP ranged from 98.5% to 111.5%, with RSD values below 5%. These findings confirm the feasibility and reliability of the designed sensor for the electrochemical detection of AP in real-world water samples.

## 4. Conclusion

In conclusion, a highly sensitive and selective electrochemical sensor for AP was successfully developed using a composite of UIO-66-NH<sub>2</sub> and Ti<sub>3</sub>C<sub>2</sub>, synthesized *via* a one-step hydrothermal process. The calcination at 300 °C under argon resulted in enhanced electrochemical properties, driven by TiO<sub>2</sub> formation and increased interlayer spacing on the MXene surface. The 50% UN@Ti<sub>3</sub>C<sub>2</sub>-C electrode demonstrated excellent electrochemical activity, enabling rapid and quantitative detection of AP with a broad linear range (0.032–160  $\mu\text{M}$ ) and an ultra-low detection limit of 10 nM. The sensor's successful application in real water and pharmaceutical tablet samples highlights its practicality and potential for real-world monitoring of AP, offering a reliable and efficient approach for environmental and pharmaceutical analysis.

## Data availability

The data supporting this article have been included as part of the ESI.† Additional data that support the findings of this study are available from the corresponding author upon reasonable request.

## Conflicts of interest

The authors report no declarations of interest.

## Acknowledgements

The authors gratefully acknowledge the financial support from the National Key Research and Development Program of China Sino-Austrian intergovernmental industry-university-research cooperation project (Project No. 2022YFE0117000), the Fundamental Research Funds for the Central Universities

(HUST: YCJJ202203008), the National Natural Science Foundation of China (52171069 and 22005109), and the Open Project Program of Hubei Key Laboratory of Materials Chemistry and Service Failure (2020MCF02).

## References

- S. Sekar, J.-S. Yun and S. Lee, *Environ. Res.*, 2023, **239**, 117293.
- F. S. Larsen and J. Wendon, *Intensive Care Med.*, 2014, **40**, 888–890.
- Y. Yan, Z. Liu, P. Xie, S. Huang, J. Chen, F. Caddeo, X. Liu, Q. Huang, M. Jin and L. Shui, *J. Colloid Interface Sci.*, 2023, **634**, 509–520.
- R. Clark, V. Borirakchanyavat, A. Davidson, R. Williams, R. Thompson, B. Widdop and R. Goulding, *Lancet*, 1973, **301**, 66–70.
- P. T. T. Ninh, N. D. Dat, M. L. Nguyen, N. T. Dong, H.-P. Chao and H. N. Tran, *Environ. Res.*, 2023, **218**, 114927.
- N. O. Erhunmwunse, I. Tongo and L. I. Ezemonye, *Ecotoxicol. Environ. Saf.*, 2021, **208**, 111482.
- I. Cipriani-Avila, J. Molinero, M. Cabrera, E. J. Medina-Villamizar, M. V. Capparelli, E. Jara-Negrete, V. Pinos-Velez, S. Acosta, D. L. Andrade and M. Barrado, *Sci. Total Environ.*, 2023, **866**, 161340.
- R. Van der Oost, J. Beyer and N. P. Vermeulen, *Environ. Toxicol. Pharmacol.*, 2003, **13**, 57–149.
- G. Sivarasan, V. Manikandan, S. Periyasamy, M. S. AlSalhi, S. Devanesan, P. S. M. Kumar, R. Rao Pasupuleti, X. Liu and H.-M. Lo, *Environ. Res.*, 2023, **227**, 115723.
- D. Tonoli, E. Varesio and G. Hopfgartner, *J. Chromatogr. B: Anal. Technol. Biomed. Life Sci.*, 2012, **904**, 42–50.
- A. Trettin, A. A. Zoerner, A. Böhmer, F.-M. Gutzki, D. O. Stichtenoth, J. Jordan and D. Tsikas, *J. Chromatogr. B: Anal. Technol. Biomed. Life Sci.*, 2011, **879**, 2274–2280.
- A. R. Khaskheli, A. Shah, M. I. Bhangar, A. Niaz and S. Mahesar, *Spectrochim. Acta, Part A*, 2007, **68**, 747–751.
- T. S. H. Pham, P. J. Mahon, G. Lai, L. Fu, C. T. Lin and A. Yu, *Electroanalysis*, 2019, **31**, 1758–1768.
- R. Manjunatha, D. H. Nagaraju, G. S. Suresh, J. S. Melo, S. F. D'Souza and T. V. Venkatesha, *Electrochim. Acta*, 2011, **56**, 6619–6627.
- T. Iftikhar, A. Aziz, G. Ashraf, Y. Xu, G. Li, T. Zhang, M. Asif, F. Xiao and H. Liu, *Food Chem.*, 2022, **395**, 133642.
- M. C. N. Ngwem, J. C. Kemmegne-Mbouguen, H. W. Langmi, N. M. Musyoka and R. Mokaya, *ChemistrySelect*, 2022, **7**, e202202308.
- S. B. Matt, S. Raghavendra, M. Shivanna, M. Sidlinganahalli and D. M. Siddalingappa, *J. Inorg. Organomet. Polym. Mater.*, 2021, **31**, 511–519.
- X. Kang, J. Wang, H. Wu, J. Liu, I. A. Aksay and Y. Lin, *Talanta*, 2010, **81**, 754–759.
- M. J. Ahmed, S. Perveen, S. G. Hussain, A. A. Khan, S. M. W. Ejaz and S. M. A. Rizvi, *Chem. Pap.*, 2023, **77**, 2275–2294.

- 20 A. U. Alam, Y. Qin, M. M. Howlader, N.-X. Hu and M. J. Deen, *Sens. Actuators, B*, 2018, **254**, 896–909.
- 21 M. Kenarkob and Z. Pourghobadi, *Microchem. J.*, 2019, **146**, 1019–1025.
- 22 P. K. Kalambate, Dhanjai, A. Sinha, Y. Li, Y. Shen and Y. Huang, *Microchim. Acta*, 2020, **187**, 1–12.
- 23 E. Mari, M. Duraisamy, M. Eswaran, S. Sellappan, K. Won, P. Chandra, P.-C. Tsai, P.-C. Huang, Y.-H. Chen and Y.-C. Lin, *Microchim. Acta*, 2024, **191**, 1–14.
- 24 Y. Li, Y. Shen, Y. Zhang, T. Zeng, Q. Wan, G. Lai and N. Yang, *Anal. Chim. Acta*, 2021, **1158**, 338419.
- 25 A. Mir, M. Shabani-Nooshabadi and N. Ziaie, *Chemosphere*, 2023, **338**, 139427.
- 26 J. Tang, Z.-Z. Hui, T. Hu, X. Cheng, J.-H. Guo, Z.-R. Li and H. Yu, *Rare Met.*, 2022, **41**, 189–198.
- 27 C. Wang, X. Liu, N. K. Demir, J. P. Chen and K. Li, *Chem. Soc. Rev.*, 2016, **45**, 5107–5134.
- 28 R. Rani, A. Deep, B. Mizaikoff and S. Singh, *J. Electroanal. Chem.*, 2022, **909**, 116124.
- 29 T. Zhang, H. Guo, J. Zhang, L. Sun, Z. Pan, B. Liu and W. Yang, *J. Electrochem. Soc.*, 2022, **169**, 016517.
- 30 J. Pan, S. Li, L. Zhang, F. Li, Z. Zhang, T. Yu and D. Zhang, *J. Energy Storage*, 2022, **55**, 105415.
- 31 Y. Li, Y. Liu, Z. Wang, P. Wang, Z. Zheng, H. Cheng, Y. Dai and B. Huang, *Chem. Eng. J.*, 2021, **411**, 128446.
- 32 L. Zhang, C. Li, Y. Chen, S. Li, F. Li, X. Wu, T. Gui, Z. Cao and Y. Wang, *Microchim. Acta*, 2023, **190**, 267.
- 33 F. Zhao, Y. Yao, C. Jiang, Y. Shao, D. Barceló, Y. Ying and J. Ping, *J. Hazard. Mater.*, 2020, **384**, 121358.
- 34 J. Zhang, S. Xu, W. Liu, Q. Wang and J. Qu, *Talanta*, 2024, **275**, 126192.
- 35 F. Liu, A. Zhou, J. Chen, J. Jia, W. Zhou, L. Wang and Q. Hu, *Appl. Surf. Sci.*, 2017, **416**, 781–789.
- 36 H. Wang, Y. Wu, J. Zhang, G. Li, H. Huang, X. Zhang and Q. M. L. Jiang, *Mater. Lett.*, 2015, **160**, 537–540.
- 37 P. A. Maughan, V. R. Seymour, R. Bernardo-Gavito, D. J. Kelly, S. Shao, S. Tantisriyanurak, R. Dawson, S. J. Haigh, R. J. Young and N. Tapia-Ruiz, *Langmuir*, 2020, **36**, 4370–4382.
- 38 Z. Man, Y. Meng, X. Lin, X. Dai, L. Wang and D. Liu, *Chem. Eng. J.*, 2022, **431**, 133952.
- 39 R. Kang, Z. Zhang, L. Guo, J. Cui, Y. Chen, X. Hou, B. Wang, C.-T. Lin, N. Jiang and J. Yu, *Sci. Rep.*, 2019, **9**, 9135.
- 40 W. Zhong, J. Zou, Q. Yu, Y. Gao, F. Qu, S. Liu, H. Zhou and L. Lu, *Food Chem.*, 2023, **402**, 134379.
- 41 J. Wang, Q. Xu, Y. Yang, J. Liu, W. Kong and L. Shi, *Talanta*, 2024, **268**, 125344.
- 42 M. Liu, Z. Zhang, M. Yang, P. Li, Y. Wang, Y. He and J. Yuan, *Composites, Part A*, 2022, **161**, 107122.
- 43 M. Peñas-Garzón, M. J. Sampaio, Y. L. Wang, J. Bedia, J. J. Rodriguez, C. Belver, C. G. Silva and J. L. Faria, *Sep. Purif. Technol.*, 2022, **286**, 120467.
- 44 J. Dong, X. Li, L. Wen, Y. Ma, J. Xu, H. Luo, J. Hou, C. Hou and D. Huo, *Food Chem.*, 2024, **437**, 137835.
- 45 S. Chen, M. Zhang, H. Zhang, X. Yan, J. Xie, J. Qi, X. Sun and J. Li, *Environ. Res.*, 2021, **201**, 111500.
- 46 X. Kong, Y. Wang, Q. Zhang, T. Zhang, Q. Teng, L. Wang, H. Wang and Y. Zhang, *J. Colloid Interface Sci.*, 2017, **505**, 615–621.
- 47 E. Laviron, *J. Electroanal. Chem. Interfacial Electrochem.*, 1979, **101**, 19–28.
- 48 J. R. Santos, D. S. Viégas, I. C. B. Alves, A. D. Rabelo, W. M. Costa, E. P. Marques, L. Zhang, J. Zhang and A. L. Marques, *Electrocatalysis*, 2019, **10**, 560–572.
- 49 M. S. Kondawar, R. R. Shah, J. J. Waghmare, N. Shah and M. K. Malusare, *Int. J. PharmTech Res.*, 2011, **3**, 1603–1608.
- 50 T. Belal, T. Awad and R. Clark, *J. Chromatogr. Sci.*, 2009, **47**, 849–854.
- 51 J. Meyer and U. Karst, *Chromatographia*, 2001, **54**, 163–167.
- 52 A. A. Mouhamed, B. M. Eltanany, N. M. Mostafa and A. H. Nadim, *J. Chromatogr. Sci.*, 2024, **62(7)**, 627–634.
- 53 T. A. Fernandes, J. P. Aguiar, A. I. Fernandes and J. F. Pinto, *J. Pharm. Anal.*, 2017, **7**, 401–405.
- 54 K. Yang, H. Yang, Y. Zheng, H. Chen, W. Liu and X. Yang, *Microchem. J.*, 2024, 110874.
- 55 S. Chen, C. Wang, M. Wang, L. Pan, D. Xu and J. Li, *J. Environ. Chem. Eng.*, 2024, **12**, 113448.
- 56 C. Liu, N. Zhang, X. Huang, Q. Wang, X. Wang and S. Wang, *Microchem. J.*, 2021, **161**, 105719.
- 57 Y. Zhang, X. Jiang, J. Zhang, H. Zhang and Y. Li, *Biosens. Bioelectron.*, 2019, **130**, 315–321.
- 58 E. Mari, M. Duraisamy, M. Eswaran, S. Sellappan, K. Won, P. Chandra, P.-C. Tsai, P.-C. Huang, Y.-H. Chen and Y.-C. Lin, *Microchim. Acta*, 2024, **191**, 212.
- 59 X. He, F. Yin, X. Yi, T. Yang, B. Chen, X. Wu, S. Guo, G. Li and Z. Li, *ACS Appl. Mater. Interfaces*, 2022, **14**, 26571–26586.
- 60 J. Hajek, M. Vandichel, B. Van de Voorde, B. Bueken, D. De Vos, M. Waroquier and V. Van Speybroeck, *J. Catal.*, 2015, **331**, 1–12.